

www.acsami.org Research Article

Durability and Degradation Mechanisms of Antifrosting Surfaces

Muhammad Jahidul Hoque,[#] Xiao Yan,*^{,#} Haoyun Qiu,[#] Yimeng Qin, Xuzhi Du, Jackson Stermer, and Nenad Miljkovic^{*}



Cite This: ACS Appl. Mater. Interfaces 2023, 15, 13711–13723



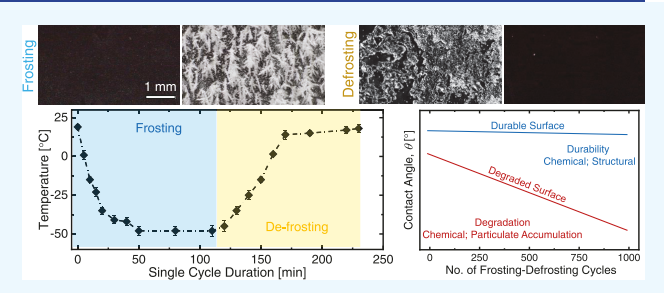
ACCESS

Metrics & More

Article Recommendations

Supporting Information

ABSTRACT: Rapid implementation of renewable energy technologies has exacerbated the potential for economic loss and safety concerns caused by ice and frost accretion, which occurs on the surfaces of wind turbine blades, photovoltaic panels, and residential and electric vehicle air-source heat pumps. The past decade has seen advances in surface chemistry and micro- and nanostructures that can promote passive antifrosting and enhance defrosting. However, the durability of these surfaces remains the major obstacle preventing real-life applications, with degradation mechanisms remaining poorly understood. Here, we conducted durability tests



on antifrosting surfaces, including superhydrophobic, hydrophobic, superhydrophilic, and slippery liquid-infused surfaces. For superhydrophobic surfaces, we demonstrate durability with progressive degradation for up to 1000 cycles of atmospheric frosting—defrosting and month-long outdoor exposure tests. We show that progressive degradation, as reflected by increased condensate retention and reduced droplet shedding, results from molecular-level degradation of the low-surface-energy self-assembled monolayer (SAM). The degradation of the SAM leads to local high-surface-energy defects, which further deteriorate the surface by promoting accumulation of atmospheric particulate matter during cyclic condensation, frosting, and melt drying. Furthermore, cyclic frosting and defrost tests demonstrate the durability and degradation mechanisms of other surfaces to show, for example, the loss of water affinity of superhydrophilic surfaces after 22 days due to atmospheric volatile organic compound (VOC) adsorption and significant lubricant drainage for lubricant-infused surfaces after 100 cycles. Our work reveals the degradation mechanism of functional surfaces during exposure to long-term frost—defrost cycling and elucidates guidelines for the development of future surfaces for real-life antifrosting/icing applications.

KEYWORDS: functional, structured, coating, superhydrophobic, durable, frost-defrost, cycles, dust

■ INTRODUCTION

Frost formation and accretion on various infrastructures are ubiquitous. Frost is usually formed through two different modes. The first mode, known as desublimation, occurs when frost accumulates on a surface through a direct vapor-solid phase transition. The second mode, known as condensation frosting, is more common and occurs when vapor undergoes a continuous transition from vapor to condensed water and eventually to a frozen solid state. Prolonged accretion of frost causes economic losses amounting to billions of dollars every year worldwide. Frost accretion can cause inefficient operation of numerous applications such as power lines, telecommunication networks, aviation systems, refrigeration systems, heat pumps, hydropower installations, wind power systems, oil rigs, cooling devices, and cryogenic systems. 3-8 Accumulation of ice on airplane wings can significantly alter the dynamic characteristics of aircraft flight, causing severe damage and even plane crashes.9 The heavy load of frost/ice on transmission lines, wind turbines, and solar panels can cause power outages over vast areas and pose a severe threat to human lives. $^{10-12}$ Frost accumulating on refrigeration equipment can reduce heat transfer efficiency by as much as 5075%, 9,13,14 resulting in significant economic losses, making defrosting a required engineering protocol.

To overcome this multibillion-dollar challenge, active or passive approaches exist to enable defrosting. ¹⁵ Active defrosting methods involve thermal, mechanical, and chemical frost/ice removal from surfaces. However, these methods tend to be expensive, energy- or resource-intensive, and/or cause environmental pollution. ^{9,16} In contrast, passive methods normally rely on antifrosting coatings that, once applied to the surface, either prevent (or reduce) frost accretion or significantly reduce frost adhesion strength. ^{15,17–19} Naturally, coatings that do not need any additional energy and cost until they reach their service life have become a very attractive approach to reduce frost accretion and/or frost—substrate

Received: December 5, 2022 Accepted: February 14, 2023 Published: March 2, 2023





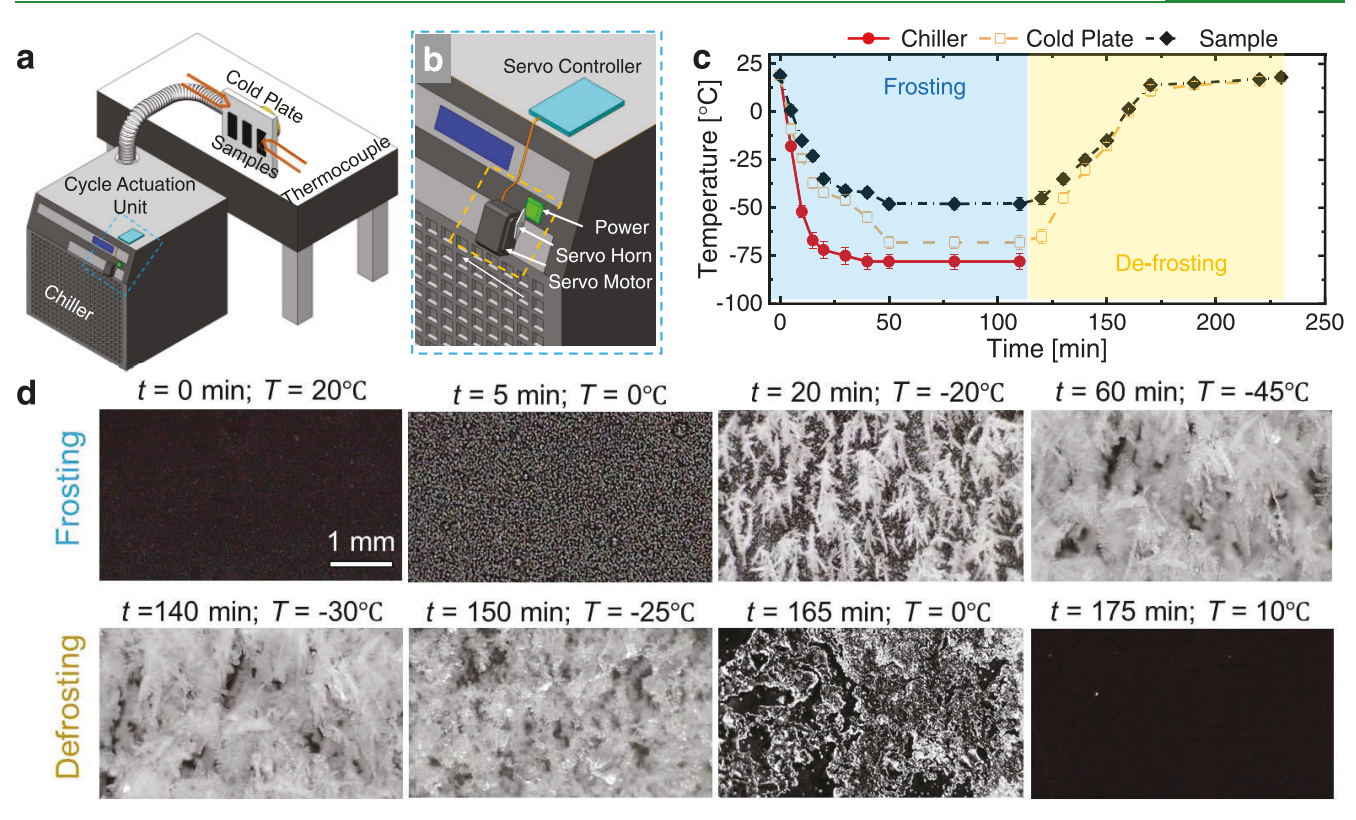


Figure 1. Long-term frosting-defrosting experiments. Three-dimensional (3D) schematic of the (a) experimental setup used for frostingdefrosting cycling experiments and (b) cycling experiment controller showing the automated chiller power actuation via servo horn. (c) Temperature profile of the system and surfaces during a single frosting-defrosting cycle. (d) Time-lapse images of a single cycle frostingdefrosting experiment on a superhydrophobic (SHPo) surface. The scale bar in the first image in (d) applies to all of the images.

adhesion strength on outdoor surfaces. The last few decades have seen unprecedented advances in the fields of surface chemistry and micro/nanofabrication, enabling the development of functional surfaces that promote facile defrosting.

In addition to smooth hydrophobic coatings (e.g., polymers) that are naturally expected to reduce frost adhesion, structured hydrophobic surfaces (superhydrophobic, SHPo) have shown outstanding frost-reduction performance due to the increased energy barrier for ice nucleation $^{20-22}$ and reduced contact angle hysteresis and ice-adhesion strength of the frost once it inevitably forms. ^{23–29} Icephobicity has been attributed to the numerous air pockets sustained within the micro- and nanostructures that minimize contact area and reduce surface energy.³⁰ For these surfaces to work, adhesion reduction arises due to the air layer trapped in the rough surface structure and comprising ~90% of the water/ice interface (the other ~10% being the solid-water or solid-ice interface). Furthermore, even if nucleation does occur, the air trapped at the solidliquid interface reduces the actual ice or frost-coated surface area and disrupts the bonding by creating stress concentrations.31 Thus, the adhesion forces are significantly weakened, which decreases the amount of energy required to keep the protected surface free of ice by up to 80%.³² Moreover, recently, researchers have demonstrated that coalescence-induced droplet jumping on ultralow-adhesion SHPo surfaces can delay condensation frosting.³¹ Droplet jumping enables condensing droplets during condensate frosting to escape at micrometric length scales ($\sim 1 \mu m$) prior to supercooling and freezing on the surface. 31,33 In addition to jumping droplet condensate removal prior to freezing, studies have shown SHPo surfaces to facilitate

delayed freezing of individual droplets, 34-36 as well as bulk water layers due to the delay in ice nucleation and higher thermal resistance at the liquid-solid interface. 37,38

Although highly promising, micro- and nanostructures also have the potential to induce mechanical interlocking due to frost nucleation within the textures, 30 which can result in deterioration in antifrosting performance of SHPo surfaces in humid environments. ^{39–41} Moreover, few studies have focused on the short-term frosting-defrosting durability of certain SHPo surfaces, showing either difficulty in sustaining surface structures⁴² or degradation of the top hydrophobic chemistry^{27,43,44} during cycling experiments. Unfortunately, studies on the long-term durability (multimonth and hundreds of frost-defrost cycles) of the antifrosting properties of SHPo surfaces have not been explored. As SHPo coatings are still widely considered and developed as a remedy to the detrimental effects of frosting, we study the long-term durability of SHPo surfaces during exposure to 1000 frosting-defrosting cycles. In addition, we examine the applicability of these SHPo surfaces in outdoor environments by performing weathering tests. After conducting a thorough study of the wetting change of the SHPo surfaces, we propose and examine the degradation mechanisms of these surfaces. In addition, we also conducted cyclic durability tests of a wide range of alternative antifrosting surfaces, including hydrophobic, superhydrophilic, and slippery liquid-infused surfaces, to investigate structural/chemical robustness and degradation mechanism. Our work presents a synergistic combination of long-term performance evaluation and mechanistic understanding of the degradation behavior of functional surfaces during frost-defrost cycling. Furthermore, our work not only

provides fundamental insights into the mechanisms of frost-defrost-induced degradation of the functional surfaces but also proposes robustness improvement guidelines for functional surfaces of the future.

RESULTS

Cyclic Frosting-Defrosting. To conduct frostingdefrosting experiments, we used a low-temperature chiller (P10N9E403BR, PolyScience) with a customized actuation unit (Figure 1a,b) (see the Methods section). Test samples were attached to the cold stage of the chiller using doublesided tape (S-14668, Uline; thickness, \sim 350 μ m) (Figure 1a), and two thermocouples (CHAL-002, Omega) were attached to the cold stage and sample surface by Kapton tape (KPT2-1/ 2,BERTECH) (Figure 1a) to monitor the temperature. The actuation unit consists of a servo controller, a motor, and a horn (Figure 1a,b). With the aid of the servo horn, the chiller power was controlled for long-term cycling experiments (Figure S1, Supporting Information). First, the chiller was connected to the power supply. Then, the servo controller was powered on, and the servo motor actuated the chiller by pushing the power button via a servo horn. After taking approximately 1 h to reach the lowest temperature of the chiller (approximately -80 °C), the chiller was maintained at that temperature for another hour to complete the frosting cycle (Figure 1c) and to grow the frost to an estimated thickness of 8 mm. Then, the servo motor again actuated the horn to turn off the chiller to initiate the defrosting cycle. The duration of the defrosting cycle was approximately 2 h, where the first hour melts the frost by room-temperature ambient heating, and the second hour allows the shedding of the melt and natural evaporation of remnant condensate to reduce water retention and refrosting before the initiation of the next frosting cycle (Figure 1c). These steps of frosting-defrosting were repeated in cycles to conduct long-term durability experiments. Figure 1d shows the exemplary time-lapse images of a frosting-defrosting cycle on an SHPo surface.

To fabricate the SHPo, we used a copper sheet (Cu, 2.032 mm thick 8963K88, McMaster) as a base substrate. The fabrication process starts with cleaning the Cu tabs by dipping them for 15 min in acetone (CAS #67-64-1, Fisher Chemical), ethanol (CAS #64-17-5, Sigma-Aldrich), isopropanol (CAS #67-63-0, Fisher Chemical), and deionized (DI) water (CAS #7732-18-5, Sigma-Aldrich), in succession, followed by rinsing with DI water. The tabs were then dipped in a 2.0 M hydrochloric acid (CAS #7647-01-0, Sigma-Aldrich) solution for 2 min to remove the native oxide layer on the surface, then rinsed multiple times with DI water, and afterward dried with a clean nitrogen gas stream. Afterward, dense bladelike nanostructured CuO surfaces were formed by immersing the cleaned tabs into a hot (90 ± 5 °C) alkaline bath of NaClO₂ (CAS #7758-19-2, Sigma-Aldrich), NaOH (CAS #1310-73-2, Sigma-Aldrich), Na₃PO₄·12H₂O (CAS #10101-89-0, Sigma-Aldrich), and DI water (3.75:5:10:100 wt %).45,46 The CuO nanostructured surfaces were then cleaned by rinsing with DI water and drying with a stream of nitrogen. They were then treated with an air plasma (PDC-001-HP from Harrick Plasma) with a power of 30 W for 3-5 min to further clean and activate the substrate. Air plasma cleaning has been shown to increase the number of hydroxyl groups on the substrate, thus enhancing coating adhesion during surface functionalization. 47 Then, the SHPo surface was developed by functionalizing the air plasma-cleaned CuO nanostructured sample using atmospheric pressure chemical vapor deposition (CVD) of a fluorinated silane ((heptadecafluoro-1,1,2,2 tetrahydrodecyl)-trimethoxysilane, HTMS, Gelest, CAS #83048-65-1). Reduction of humidity during the CVD step is critical for ensuring coating adherence to the substrate. In our experiments, we achieved this by preheating the beaker and sample in the furnace at ~ 80 °C for 15 min prior to conducting the CVD process.

The SHPo surface experiences condensation frosting, which consists of several subsequent events: supercooled condensation, onset of freezing, frost halo formation, interdroplet ice bridging, cluster formation, and frost densification. 1,51 During supercooled condensation, as the substrate temperature reaches below the dew point (~10 °C) and the ambient atmosphere reaches the required degree of supersaturation, atmospheric water vapor nucleates heterogeneously on the substrate and supercooled water droplets keep growing from the ambient vapor. Once the substrate reaches the subzero temperature and overcomes the ice nucleation energy barrier, the onset of freezing and frost halo formation begins. 51 This is followed be newly frozen water droplets harvesting water from their adjacent water droplets and growing ice bridges toward them. 52 Finally, once the global freeze front has propagated through the entire condensate population, a network of interconnected frozen droplets provides the foundation upon which out-of-plane frost (dendrite) growth can happen.

As shown in Figure 1d, during the early stages of the cyclic experiment $(t = 5 \text{ min}; T = 0 ^{\circ}\text{C})$, small subcooled droplets cover the surface. At later times, due to increased subcooling, droplets freeze, form bridges, and frost grows out-of-plane and densifies. Once the frosting phase of the cycle is complete, the total frost thickness is estimated to be \sim 8.2 \pm 1.3 mm using optical imaging from the side. The ambient heated defrosting process involves top-down melting, where the accumulated frost always melts from the free interface between air and frost. Melting begins at the tips of the frost dendrites due to the absorption of heat from the ambient air. Once all of the dendrites on the surface have melted, in-plane frost begins to melt. Over time, the thickness of the frost layers gradually decreases, and highly mobile slush regions are visible all over the surface. As shown in Figure 1d, at t = 165 min and T = 0°C, we observed the removal of slush-inducing shear force on the surface. Due to the nature of the SHPo surface, after completing the defrosting cycle, condensate retention on the surface was not observed. However, the surface was maintained at room temperature for another hour to allow for any trapped microdroplet evaporation. The complete removal of any meltwater from the surface was particularly important as it prevents a phenomenon called refrosting. Refrosting occurs when meltwater retaining on the surface provides active nucleation sites for frost formation in subsequent frost cycles and acts to alter the nature of the frost layer, as well as the final frost thickness, as the number of cycles proceeds beyond the initial cycle. 53,54 To avoid these confounding experimental parameters, refrosting was avoided in these experiments. To assess long-term durability, we conducted the experiment for a total of 1000 frosting-defrosting cycles; this duration was chosen to simulate the practical usage of antifrosting surfaces in real-world situations, such as supermarket display cases that require periodic defrosting with 2-4 cycles per day. 55,56 The 1000 cycles equated to a display case operating for approximately 3 years if defrosted once per day or 9 months if defrosted four times per day. Thus, our experiment provided

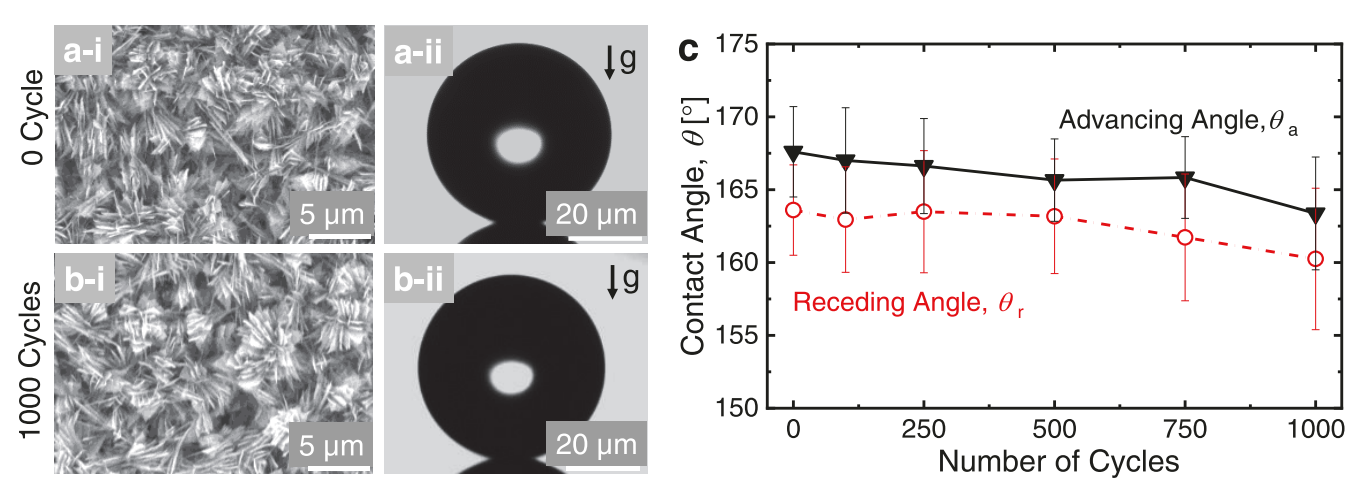


Figure 2. Surface wettability and structure robustness after 1000 frosting—defrosting cycles. (a, b) Scanning electron microscopy images and DI water droplet formation behaviors of a fresh SHPo surface and a 1000-cycle tested SHPo surface. (c) Apparent advancing and receding DI water droplet contact angles of the SHPo surface during the cycling experiments. The results showed no significant change in wettability, proving reasonably good robustness of the hydrophobic chemistry and the surface structure.

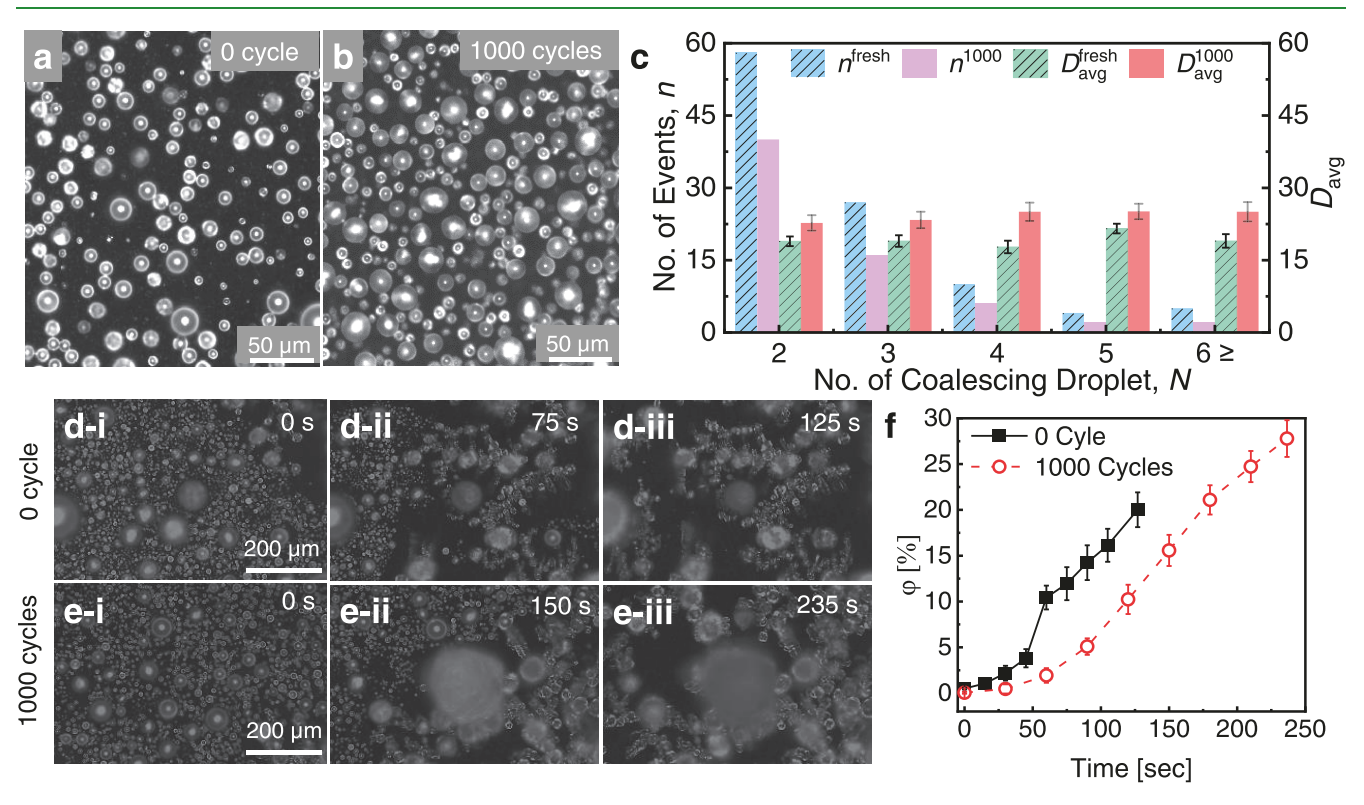


Figure 3. SHPo surface characterization after 1000 frost—defrost cycles. Top-view optical images of atmospheric water vapor condensation on a (a) fresh sample and (b) 1000-cycled SHPo CuO sample. (c) Comparison of the number of jumping events (n) and average diameter of participating droplets (D_{avg}) for the fresh and cycled samples as a function of the number of coalescing droplets (N). Time-lapse images of frost propagation on a (d) fresh sample and (e) cycled sample showing (f) higher frost coverage on the cycled sample when compared to the fresh sample.

a prediction of the multimonth performance of antifrosting surfaces under real-world conditions.

During the frosting/defrosting cycles, surface nanostructures may experience forces resulting from the volumetric expansion of freezing droplets and shear forces induced by the shedding of frost/melt. To evaluate micro/nanostructure robustness of the CuO-based SHPo surface, we conducted scanning electron microscopy (SEM) and compared the result with that of a fresh surface (0 cycle) (see the Methods section). The SEM images of the SHPo sample show undamaged CuO micro-

blades even after 1000 test cycles (Figure 2a,b), proving the robustness of the surface structure. To characterize the surface wettability change after conducting the cycling experiments, deionized (DI) water droplet contact angles were measured using a microgoniometer (MCA-3, Kyowa Interface Science), where liquid droplets (100 nL) were dynamically grown to measure the apparent advancing contact angles (see the Methods section). The microgoniometer droplet dispenser was then turned off, and the deposited droplets were allowed to continuously evaporate to obtain the apparent receding contact

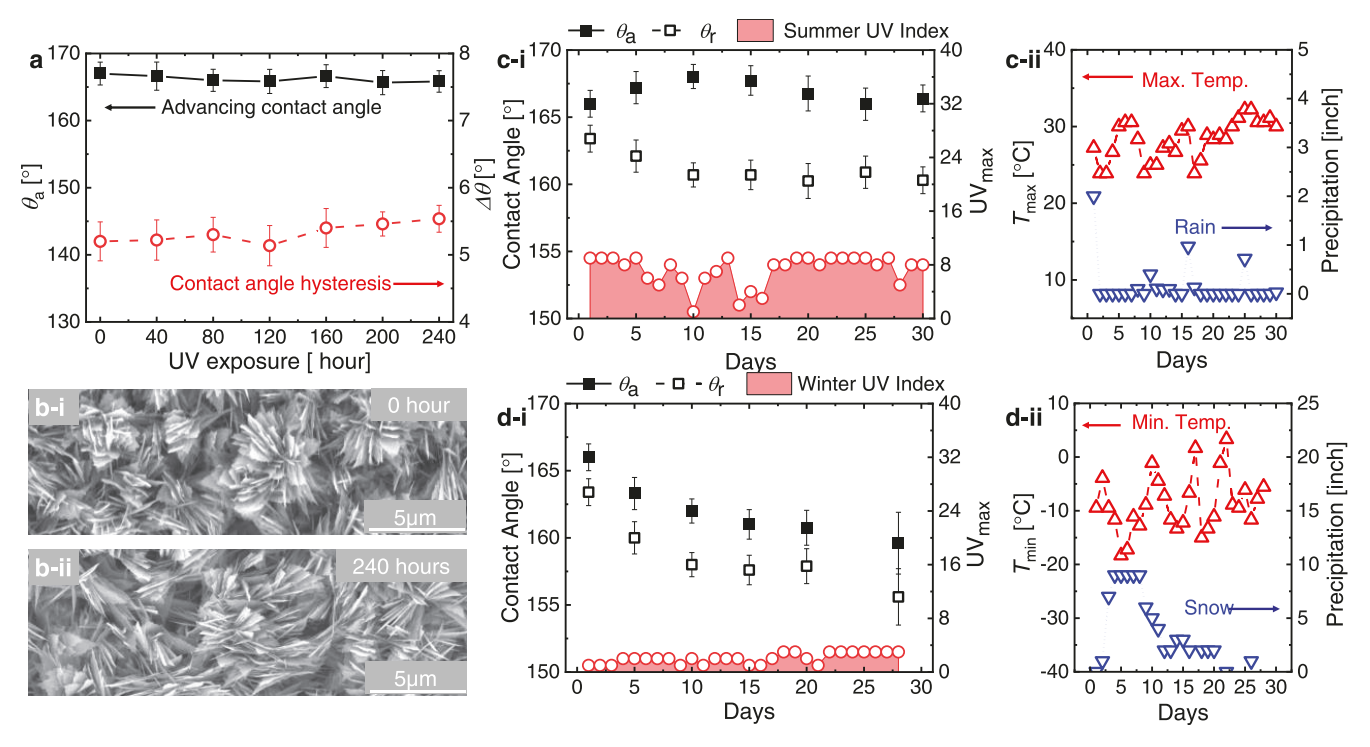


Figure 4. Robustness of the SHPo surface to UV and outdoor conditions. (a) DI water droplet contact angle on the SHPo surface after 240 h (equivalent to 1 month of testing, assuming 8 h full sunlight/day) of UV exposure. (b) SEM images of the (i) fresh and (ii) tested samples, showing no apparent damage to the surface structures. Changes in DI water contact angles of the SHPo samples exposed to (c-i) summer (July 2021) and (d-i) winter (February 2022) weather. Maximum UV index data plotted in (c-i) and (d-i) are obtained from the National Weather forecast for Urbana, Illinois, USA. During summer (July 2021), in addition to sunlight, the samples experienced (c-ii) rain for a few days, while in the winter (February 2022), the samples faced (d-ii) low temperatures and heavy snow.

angles. 47,57 Alike the observed structural integrity, the droplet surface interaction remained similar after 1000 cycles (Figure 2a-ii,b-ii). A slight change in the apparent contact angle and contact angle hysteresis (Figure 2c) indicated reasonable chemical robustness of the functional HTMS layer.

Antifrosting Performance Degradation. Long-term frost-defrost cycling experiments did not show a significant change in wettability or visible mechanical damage of the CuO surface structures. To evaluate droplet dynamics of the cycle tested (1000 frosting-defrosting cycles) SHPo samples, we performed atmospheric water vapor condensation and frosting characterization and compared with a fresh sample (0 frostdefrost cycle). Experiments were conducted on a customized top-view optical microscopy setup (see the Methods section). 47,58 Although the condensation behavior looks similar (Figure 3a,b), quantification of the cycles sample showed a reduced number of jumping droplet events (Figure 3c). For binary (N = 2) droplet coalescence jumping, we observed a \sim 30% reduction in jumping events for the cycled samples in comparison with the fresh SHPo surface. This jumping droplet reduction resulted in a ~20% increase in average droplet size involved in coalesce phenomena. For multidroplet jumping, the cycled samples showed a gradual decrease in jumping events. We hypothesize that this resulted from the molecularlevel degradation of the low-surface-energy self-assembled monolayer (SAM) mediated by long-term exposure to the humid environment. 49,50 SAM degradation leads to reduced local and global hydrophobicity, which further leads to the accumulation of atmospheric particulate matter (volatile organic compounds (VOCs) and dust) during condensation/ frosting/defrosting/evaporation cycles.⁵⁹ During frosting,

particulate matter from the atmosphere accumulates on the defect sites (slowly degrading SAM locations) and inside the CuO cavities along with the atmospheric water vapor condensate. During the defrosting cycle, while the meltwater sheds from the surface, some of these microscale particles stick to the surface depending on the nature of the particle—surface interaction. Long-term exposure to frost-defrost cycling increases the SAM degradation rate and density of the particles on the surface, which act as droplet nucleation and pinning sites. These sites increase the droplet-surface adhesion, resulting in reduced coalescence-induced droplet jumping (Figure 3c).

We also conducted atmospheric water vapor condensationfrosting experiments on the SHPo samples using the same microscopy setup. As shown in Figure 3d,e, compared to the fresh sample, the 1000-cycled sample showed higher frost coverage due to the accumulation of the particulate matter. Surfaces exposed to 1000 frosting-defrosting cycles showed a ~7% higher frost coverage compared to the fresh SHPo surface (Figure 3f). Due to the presence of more pinning sites (microand nanoagglomerates) on the cycled sample, the condensate size is relatively larger, which eventually leads to reduced droplet jumping and higher frost coverage. However, due to the presence of agglomerates and delayed onset of frost nucleation, ice bridging occurs at a reduced rate, resulting in slower frost propagation on the cycled sample. Details of the condensation and frosting experiments and the process of calculating the frost area coverage are added to Section S2 of the Supporting Information.

Outdoor Exposure Testing. While in operation, structured SHPo surfaces can have two main modes of degradation,

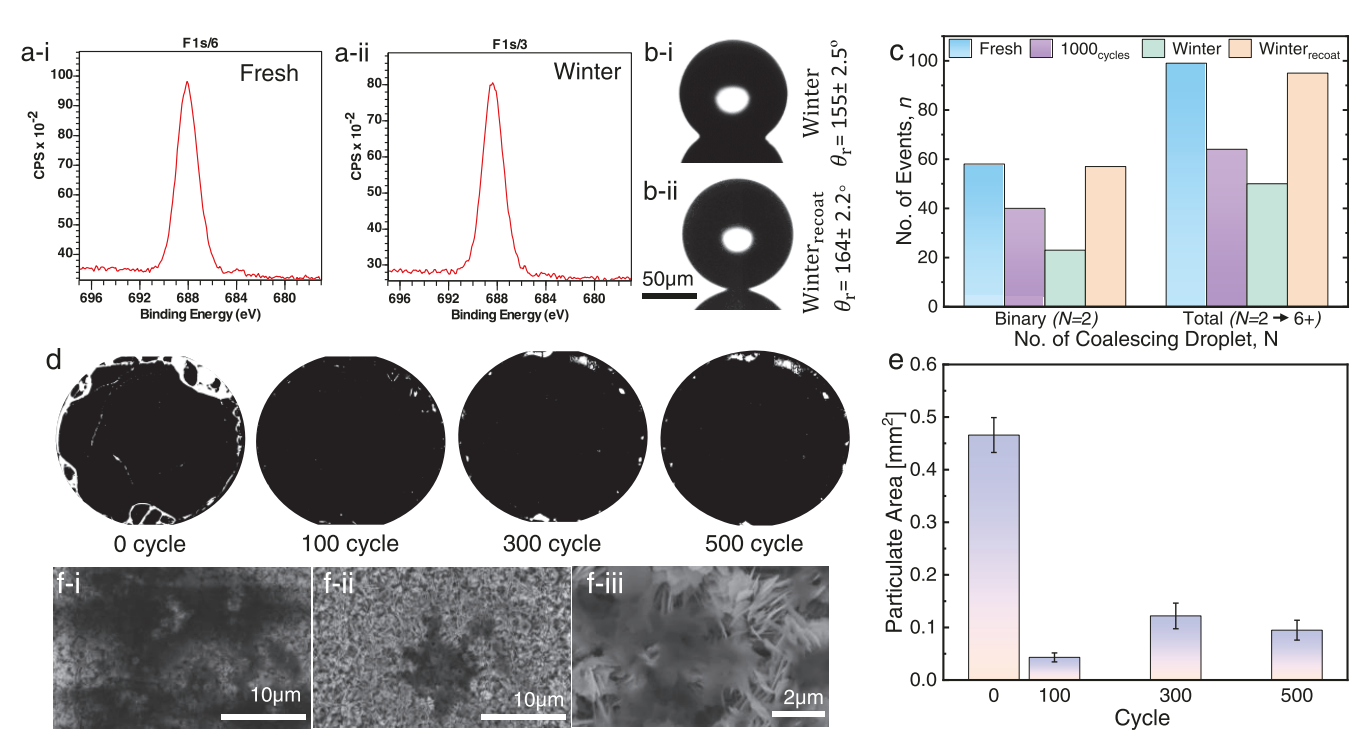


Figure 5. Surface wetting property change and degradation mechanism of SHPo surfaces. (a) Comparison of XPS analysis of a fresh and winter-exposed SHPo surface. (b) Receding DI water contact angle of a winter-exposed and winter-exposed-recoated surface showing recovery of hydrophobicity after recoating with HTMS. (c) Comparison of jumping droplet condensation performance among surfaces. (d) Top-view optical image of a coffee ring on a SHPo surface; 0 cycle, immediately after fabrication; 100/300/500 cycles, after 100/300/500 condensation—evaporation cycles. (e) Comparison of the coffee particle agglomeration area after different condensation—evaporation cycles. After 100 cycles, particle clusters at the ring become thin because of the removal of the loosely connected particles by the condensate. For higher condensation—evaporation cycles, the coffee ring becomes thicker due to the redistribution of coffee particles arising from in-plane droplet motion. However, (f) SEM images show that clusters/particles of coffee are randomly distributed and adhered to the surface without damaging the structures. The calculation of the coffee particle area was performed by following the same process as the frost coverage calculation, as described in Section S2 of the Supporting Information.

either the hydrophobic functional coating can fail or the surface structure can be damaged. Our frost-defrost cycling experiments demonstrated that the functional coating and structural robustness of the SHPo samples in indoor environments is reasonable. However, we observed slight degradation in antifrosting performance of the surfaces. To evaluate the surface behavior in real applications, we next performed outdoor exposure testing (see the Methods section). If the SHPo surface were to be used in an outdoor heat exchanger where frosting occurs, 60-62 it would experience rain, snow, and ultraviolet (UV) light exposure, leading most likely to surface property change. In outdoor applications, surfaces experience UV exposure and daily temperature swings. Previous studies have shown that CuO functionalized with HTMS can survive in 200 °C air temperature. 57 To evaluate the functional coating (HTMS) robustness only to UV, we performed UV exposure tests by placing the samples in a UV cleaner (FB-UVXL-1000, Fisher Scientific). A glass beaker with six identical SHPo CuO coupons is placed in the UV cleaner. Throughout the experiment, the UV energy level was maintained at 9000 μ J/cm², which is ~35% higher than maximum UV radiation from sunlight at the testing site (Table S1, Supporting Information). The test was continued for 240 h, which is equivalent to 1 month of UV exposure, assuming 8 h of direct sunlight per day. After 40 h, the first sample was taken out, followed by the rest of the samples sequentially at 80, 120, 160, 200, and 240 h.

To quantify the damage of the HTMS coating and the CuO surface structure due to long-term UV exposure, the DI water droplet contact angle was measured (see the Methods section). As shown in Figure 4a, even after 240 h of UV exposure, the HTMS-coated surfaces maintain superhydrophobicity, indicating the robustness of the coating and its potential to be used in outdoor conditions. As expected, SEM of the UV-exposed sample shows unscathed CuO nanoblades, indicating structural robustness (Figure 4b). UV light comprises a segment of the electromagnetic spectrum between 400 and 100 nm wavelengths. 63 The energy of UV light can be calculated using E = hc/λ , where h is Planck's constant ($h = 6.625 \times 10^{-34} \text{ J} \cdot \text{s}$) and c is the speed of light in vacuum ($c = 3 \times 10^8 \text{ m/s}$), resulting in values of $E = 4.9 \times 10^{-19}$ J ($\lambda = 400$ nm) to $E = 1.99 \times 10^{-18}$ J ($\lambda = 100 \text{ nm}$). The chemical bond energy levels for SAM range from 5×10^{-19} J to 8×10^{-19} J (see Table S2, Supporting Information). Hence, the minimum required photon energy to break the bonds is on the order of 4.9×10^{-19} J (400 nm UV) light). As our UV exposure experiments did not show any coating damage, we can only conclude that the UV light coming from the setup was not high energy and was on a wavelength spectrum closer to 400 nm as opposed to 100 nm.

To evaluate the robustness of these surfaces in the outdoor environment, we exposed the samples to outdoor ambient conditions for one summer month (July 2021, Urbana, IL) and one winter month (February 2022, Urbana, IL). For the summer experiment, six identical SHPo CuO coupons (5 cm \times 5 cm) were attached to a 45° tilted metal plate and kept in an

open field (Urbana, Illinois) facing south. This enabled exposure to sunlight, wind, rain, snow, and dust particles from the air. Sample tilt enabled more direct sunlight exposure as well as shedding of any particulate accumulation, which increased the chance of shear induced damage of the surfaces.⁶⁴ The test was continued for a period of one month each time. After 5 days, the first sample was taken out, followed by rest sequentially at 10, 15, 20, 25, and 30 days. For the winter outdoor exposure experiment, five identical samples were used, and the same procedures and intervals were maintained until the 4th sample. As there were 28 days in February 2022, the fifth sample was taken off after an 8 day interval from the fourth sample. During the summer experiments (July 2021), the weather was sunny for the majority of the time, with low precipitation for a few days (Figure 4c-ii). The UV level, roughly quantified by the maximum UV index during each day,⁶⁵ remained high (Figure 4c-i). The UV index was low in winter (Figure 4d-i); however, the samples experienced snow accumulation and shedding in February 2022 (Urbana, IL) (Figure 4d-ii).

To characterize the wettability change of the surfaces, DI water contact angles were measured using the microgoniometer setup (see the Methods section). As shown in Figure 4c-i, wettability characterization of the summer samples showed that the CuO nanoblade surface functionalized with HTMS remained superhydrophobic throughout the entire 1 month test period, implying that the covalent bonding between the HTMS molecules and the substrate was strong enough to overcome desorption of the HTMS coating induced by exposure to outdoor weather. However, for the winter weather-exposed samples, a slight decrease in surface wettability was observed as quantified by the decreasing apparent contact angle (Figure 4d-i). This is most likely due to the heavy snow that the surfaces experienced during the test period (Figure 3d-ii), leading to frost-defrost-induced enhanced molecular-level degradation of the SAM and increased particulate matter accumulation. Moreover, due to the high density of particles in the outdoor environment when compared to the lab environment, the 1 month winter-exposed samples showed more wettability change when compared to the indoor lab experiments. Interestingly, the summer-exposed samples did not show such behavior due to the absence of moisture (low precipitation, Figure 4c-ii). Our observations showed that in frost-defrosting environments, surface damage is triggered by the combination of moisture exposure and particulate accumulation.

Degradation Mechanisms. Based on the results from our long-term frost-defrost cycling and winter outdoor weather testing, we did observe a measurable wettability change and hypothesized that it stems from molecular-level coating damage and particulate accretion. To evaluate the surface chemistry change of the tested samples, we performed X-ray photoelectron spectroscopy (XPS) and compared it with fresh samples (no cycling and/or weather exposure) (see the Methods section). Interestingly, XPS analysis did not show any significant change in hydrophobic chemistry among the surfaces (Figure S2, Supporting Information). When we compared the fresh and winter-exposed SHPo surfaces, an identical F-peak was observed (Figure 5a(i-ii), but we noticed a decrease in the receding contact angle (Figure 4d-i). We anticipated that this degradation of the surface is due to the slow hydrolysis of the hydrophobic chemistry⁵⁰ and is not strong enough to be detected by XPS. To evaluate this

hypothesis, we performed recoating experiments. We recoated the winter-exposed (the sample that experienced the most harsh environment) surface using the same atmospheric pressure chemical vapor deposition (CVD) technique of a fluorinated silane (heptadecafluorodecyltrimethoxy-silane, HTMS, Gelest, CAS #83048-65-1).48 Interestingly, after recoating the winter-tested surface, we observed similar hydrophobicity to a fresh SHPo surface, around 9° improvement of the receding contact angle (Figure 5b). To compare the surface perfromance, we performed the same microscopic atmospheric water vapor condensation experiments and compared the jumping droplet performance of the recoated surface with those of the other tested and fresh surfaces (Figure 5c). As shown in Figure 5c, the winter-exposed surface showed \sim 66% and \sim 43% reductions in binary (N = 2) droplet coalescence jumping compared to fresh SHPo and 1000-cycle tested surface, respectively. After recoating, the winter-exposed surface recovered performance and showed similar performance to a fresh surface (\sim 99% binary (N=2) jumping and ~96% total $(2 \ge N \ge 6)$ jumping events compared to the fresh surface).

Another possible route of surface degradation is particle accumulation-mediated damage of the functional surface. To test our hypothesis, we conducted a coffee ring experiment. 66,67 First, coffee powder at a ratio of 1:1000 mg was diluted in DI water and stirred for 10 min at room temperature. Then, the 2 mm diameter droplet of the coffee solution was placed on an SHPo surface and allowed to evaporate. To make sure all of the water was evaporated, we heated the surface on a hot plate at 40 °C for 30 min. Once the water completely evaporated, a fine coffee ring was visible on the surface (Figure 5d). To observe the dust accumulation/ removal mechanism, we performed atmospheric water vapor condensation-evaporation cycling experiments on the coffee ring sample using the same microscopy setup. 47,58 The experiment started at room temperature and cooling the surface to 2 °C to initiate condensate nucleation. Thereafter, the sample was held at 2 °C for 15 min, allowing condensate to grow. This resulted in in-plane (coalescence) and out-of-plane (jumping) movements of the condensate droplets. Afterward, the surface was heated to room temperature to evaporate all droplets. We performed a total of 500 condensationevaporation cycles on the coffee ring sample. Figure 5d shows that, at 0 cycle, at the periphery of the ring, there are clusters of coffee particles forming a thick coffee ring. However, after 100 cycles, these clusters become thin because of the removal of loosely connected particles by the condensate. Interestingly, after 300 and 500 cycles, we observed thickening of the ring compared to the 100-cycle image (Figure 5e). This thickening occurs due to droplet coalesce and in-plane movement of the droplets, resulting in loose particles changing location. After several cycles of coming into contact with the pinned locations at the edge of the ring, particles begin to accumulate without damaging the surface structures (Figure 5f). Although the coffee ring experiments were conducted on flat surfaces, which are different from the sample orientation of our experiments (vertical/tilted). However, a similar phenomenon occurs during frost-defrost cycling and winter weather testing due to the presence of a wet environment (condensation/frost/defrost/snow). Depending on the density of the particulate matter (dust and VOCs) in the experimental environment and the types of particulate, the surface will experience strong/weak particulate-surface

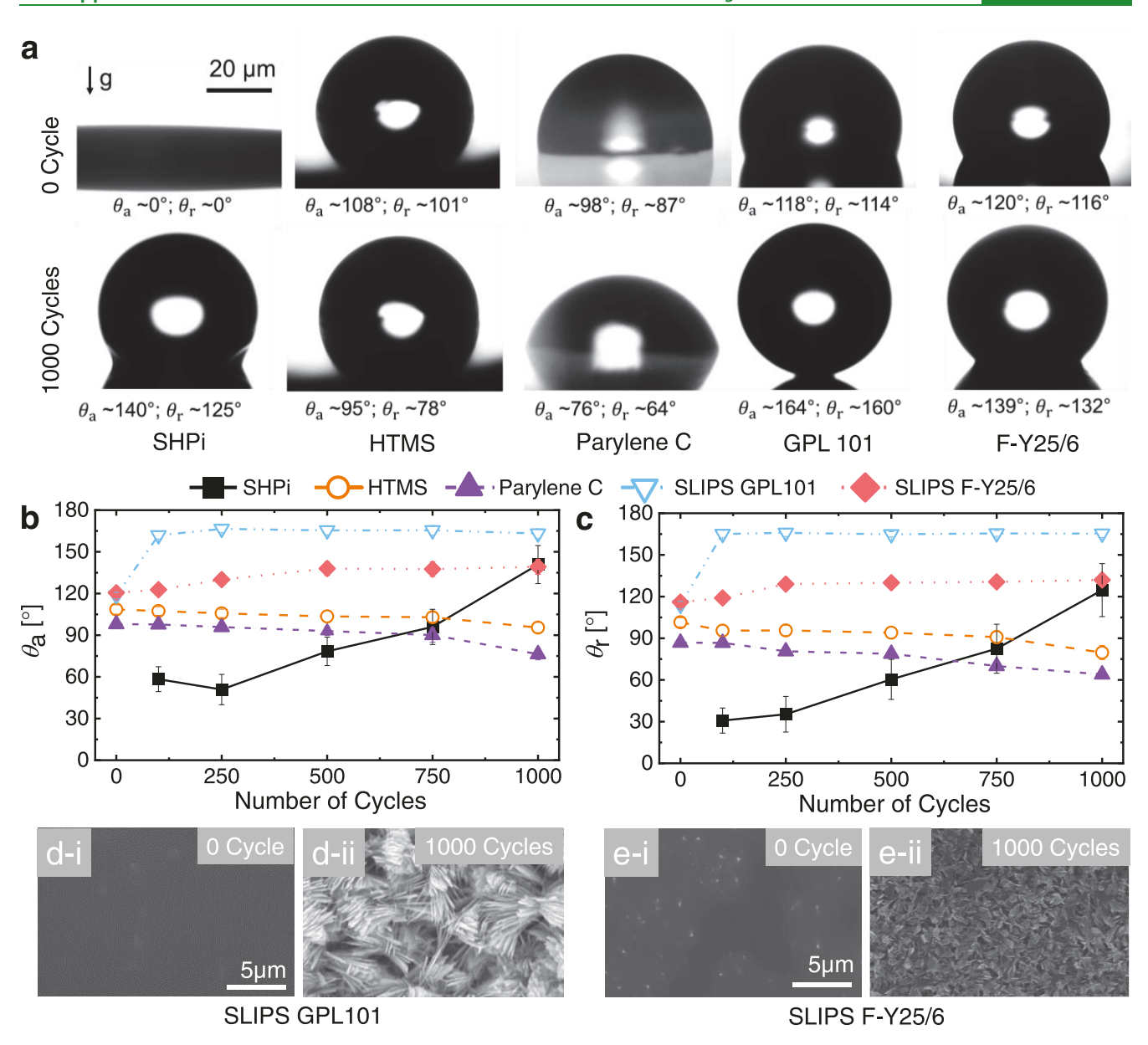


Figure 6. Performance and degradation mechanism of alternate antifrosting surfaces. (a) Optical images of DI water droplets residing on different surfaces before (top row) and after (bottom row) 1000 frost—defrost cycles. (b) Apparent advancing and (c) apparent receding DI water contact angles of the alternate functional surfaces as a function of the number of frost—defrost cycles. (d-e) SEM images of SLIPS surfaces before and after cycling.

interaction. This interaction will also be affected by the degree of coating degradation present at any location. During defrosting/desnowing, some loose particles can be washed away with the melt, while others can change location and accumulate on local defects at different places, leading to the apparent surface functionality change. From the nature of our experimental conditions, surfaces may experience slow hydrolysis of the coating and particulate accumulation. Hence, recoating the surface after a certain period of exposure not only rejuvenates the coating but also enables VOC accumulation, which leads to surface wettability recovery.

Performance of Alternate Antifrosting Surfaces. To evaluate the performance and degradation mechanism of other antifrosting surfaces, we also performed long-term frost-defrost cycling experiments on superhydrophilic (SHPi), hydrophobic (HP), and slippery liquid-infused surfaces

(SLIPS).⁶⁸ To create superhydrophilic surfaces, nonfunctionalized CuO nanoblade surfaces were used. Clean and smooth Cu samples coated with HTMS or Parylene C were used to form HP surfaces. Details of Parylene C coating and SLIPS fabrication are added in Section S5 of the Supporting Information. For SLIPS fabrication, the SHPo surfaces were infused with two oils having different properties (see Table S3, Supporting Information). Due to the variation in surface wettability of these surfaces, differences in performance and degradation mechanisms were observed after exposure to long-term cyclic experiments.

Figure 6a shows the droplet formation behaviors and water droplet apparent contact angles of the fresh and 1000-cycled samples. For the SHPi surface, although the surface structures remain unchanged (see Figure S3, Supporting Information), a sharp increase in contact angle after long-term exposure to the

frost-defrost experiment was observed (Figure 6b,c). We anticipated that this occurs due to the chemical changes on the surface after prolonged exposure to the humid environment.

X-ray photoelectron spectroscopy (XPS) analysis of the SHPi surfaces showed that the surface absorbs VOCs from the environment. 47,69 We hypothesized that VOC absorption is amplified on the SHPi surface in the wet environment during the cycling experiments. To validate the hypothesis, we performed XPS analysis on superhydrophilic surfaces after different exposure time spans in the experimental ambient. Our XPS analysis shows that the contents of C-C, C=O (Figure S4a, Supporting Information), and O-C (Figure S4b, Supporting Information) increase upon exposure to ambient air, consistent with the observation for CuO nanowire samples. 47 Both the HTMS- and Parylene C-coated HP surfaces did show slight changes in contact angle behavior after cycling (Figure 6b,c), indicating slow degradation of the surface. This is possible because of similar coating degradation to the SHPo surfaces. The SLIPS surfaces showed an increase in contact angle after exposure to cycling. At the beginning of the test, the CuO structures of the SLIPS samples were not visible due to the presence of impregnated oil layers (Figure 6d-i,e-i). However, SLIPS infused with low-viscosity oil (GPL 101) became superhydrophobic ($\theta_a \sim 160^\circ$) after ~ 100 frostdefrost cycles (Figure 6b,c) due to the depletion of infused oil during defrosting, leaving behind exposed superhydrophobic CuO structures (Figure 6d-ii). However, the F-Y25/6 SLIPS maintains its hydrophobicity with a slight increase in contact angle (Figure 6b,c) due to a slower rate of oil depletion (Figure 6e-ii). This is because F-Y2/56 has an order of magnitude higher viscosity compared to GPL 101 (see Table S2, Supporting Information). Hence, the surface slipperiness degrades at a slower rate due to less depletion of the impregnated oil layer. 57,68 Therefore, to enhance the durability of SLIPS in frost/defrost applications, it is recommended to infuse oils having high viscosities.

When evaluating the performance of SLIPS after undergoing cyclic testing, we focused on changes in wettability and structural integrity, but we did not assess lubricant drainage. This was due to the challenge of measuring small quantities of the lubricant (0.00038 g/cm² for a 2 μ m thick CuO microstructure with a solid fraction of 0.023)⁵⁷ and the high potential for measurement errors, which would have made it difficult to accurately determine the lubricant concentration.^{70,71}

DISCUSSION

Condensation-induced degradation of functional coatings is caused by blister formation due to the presence of uncontrolled pinholes on the coating and poor adhesion of the hydrophobic chemistry to the substrate.⁷² Degradation is amplified in cyclic testing due to the additionally generated shear arising from long-time in-plane droplet dynamics. In the past, short timescale (<1 month) studies have shown that condensation-evaporation cycles can induce agglomerate formation as a possible route to surface damage. 59 Unlike condensation, where continuous droplet nucleation, coalescence, and shedding generate shear stress on the surface, during frost-defrost cycling, shear force generation is not a dominant factor for surface damage. In our study, we observed that multimonth frost-defrost cycling-induced surface degradation does not damage the surface structures, but it shows very slow damage of the functional coating. Degradation

occurs mainly due to the molecular-level damage of the coating and agglomeration of particles from the ambient testing environment. Water solidification/frosting allows a longer settling time for agglomerates and may induce coating hydrolysis. During the melt/defrost period, the rate of agglomerate removal is smaller compared to the removal in the case of condensation-induced droplet shedding. Our 1000cycle test (~5.5 months) and 1 winter month test did not show any significant change in surface wettability or structural damage. However, jumping droplets and microscopic local frost dynamics showed a clear sign of performance degradation.

In the future, it would be good to study the lifespan of these functional surfaces for even longer timescales (~2 years) in a controlled colder environment. The longer run time may elucidate the presence of other degradation routes similar to condensation. Moreover, to obtain a better understanding of the degradation mechanism, it is necessary to study the surface behavior in a particulate matter-free environment. This will elucidate purely coating chemistry-mediated wettability change after long exposure to humid environments.

To test our hypothesis of surface damage, we recoated the winter-exposed surface and observed a significant improvement in surface wettability. However, to fully confirm the complete hydrolysis or global damage of surface chemistry, additional long-term outdoor or accelerated indoor cycling experiments are needed. To test our hypothesis of particulate accumulationinduced damage, we used the coffee ring effect in combination with condensation cycling. In the future, it would be interesting to conduct similar experiments considering different dust/particles covering a wide range of particle-surface adhesions. Studies focused on selecting common particles found in the atmosphere, and their interaction with the surface during cycling experiments, are also necessary. Moreover, in our study, we focused on a few selected coating chemistries. To nullify the effect of coating variation on particle accumulation, it is necessary to study a wide variety of hydrophobic chemistries. During SLIPS testing, we focused only on oil depletion-induced surface degradation during defrosting. However, the presence of oil on the structured functional surface may enhance particulate accumulation, which was not studied here in detail. Hence, further studies are needed to verify this phenomenon. Although our work showed that the wettability of both structured and smooth surfaces remained relatively unchanged during the span of the cycling tests, comparison studies are needed to understand the effect of different surface structures.

In our study, the surface temperature was maintained at approximately -45 °C during the frosting cycles. However, to evaluate the effect of surface temperature on agglomerate accumulation, it would be interesting to study surface behavior at variable supercooling and in a dust/particle-controlled environment (high and low dust densities) to further test our hypothesized degradation mechanism. To evaluate the effect of pure thermomechanical stress on the surface due to sudden temperature swings, we performed a brief thermal cycling experiment in a laboratory test chamber (WeissTechnik, LabEvent). Here, we exposed an SHPo surface in the temperature range from -45 to 150 °C for 20 cycles (Figure S5, Supporting Information). However, the coefficient of thermal expansion (CTE) mismatch between the substrate and coating was not high enough to change the surface behavior for this temperature range and experimental duration. Hence, we

did not observe any change in surface wettability and structural damage (Figure S5, Supporting Information). Future studies are needed to evaluate the surface/structure robustness after long-term (>1000 thermal cycles) exposure to harsher environments (more drastic temperature swings).

Unlike steady Joule heating, recent studies on pulseinterfacial defrosting have shown an effective route to remove frost/ice accretion from surfaces. 73,74 This active frost removal technique is rapid (timescale ~ sec) and energy-efficient. Our study focused on room-temperature heating during the defrost cycle, which has a timescale of 1 h. Faster frost removal during the defrosting cycle may lead to earlier surface damage and can change the adhesion strength of the particulate matter to the surface. It would be interesting to study the behavior of the functional surfaces integrated with pulse-interfacial defrosting for longer times in controlled environments.

In this study, all experiments were conducted in quiescent conditions. Many real-life applications, such as air-source heat pumps, utilize forced convection, which accelerates fouling and particulate accumulation. Along with frosting, particulate accumulation adds thermal insulation, restricts airflow, induces thermal stresses, and thus increases pressure drop and energy consumption of the system.⁷⁵ In the future, the performance of these surfaces and degradation mechanisms in forced convection environments is needed, where mass transfer from the atmosphere is expected to play a more important role.

CONCLUSIONS

We experimentally studied the behavior of antifrosting surfaces during long-term frost-defrost cycling. After 1000 frostingdefrosting cycles, we observed that the functional hydrophobic chemistry conformally coating the surface structures did not significantly degrade and that the CuO structures remained unscathed, leading to a limited change in wettability. Similar surface robustness was observed during lab-scale UV exposure tests. To evaluate the applicability of the SHPo antifrosting surfaces to outdoor environments having higher particulate densities, we performed weathering tests in the summer and winter months in Urbana, IL, USA. Our tests revealed that in winter, due to the longer exposure to snow, the surface wetting properties changed. However, summer testing did not show significant change. Long-term exposure to wet environments led to performance degradation of SHPo surfaces. Using binary droplet jumping as a degradation proxy, we showed that the 1000-cycled sample exhibited ~30% reduction of jumping droplet events, resulting from ~20% higher time-averaged droplet size involved in coalesce phenomena. This number of binary jumping droplet events further decreased by ~66% for winter-exposed samples. We demonstrated that these effects occur due to the slow damage of the coating and particulate accumulation on the surface. To test our hypotheses, we recoated the winter-exposed surface and observed a revival of the surface wettability and similar jumping droplet condensation performance to that of the fresh SHPo surface. Our study showed that during frost-defrost cycling, the surface does not experience structural damage; rather, degradation occurs mainly due to slow damage of the hydrophobic coating and particulate accumulation on the surface. Our work elucidated previously unexplored degradation mechanics of structured functional surfaces during exposure to long-term frost-defrost cycles. Our work also outlined future directions toward the development of next-generation durable antifrost/ dust coatings for a variety of applications.

METHODS

Frosting and Defrosting Cyclic Testing. The cyclic test involves repeated cycles of frosting and defrosting. The samples are attached to a low-temperature chiller (P10N9E403BR, PolyScience) that is controlled by a custom actuation unit. The chiller takes approximately 1 h to reach its lowest temperature of around -80 °C from room temperature and is maintained at this temperature for another hour to complete the frosting cycle. The sample temperature during the test is approximately -50 °C, and all temperatures are measured using thermocouples placed at different locations within the setup. The defrosting cycle is triggered by the actuation unit and lasts for approximately 2 h. During the first hour, the frost is melted by room-temperature ambient heating, and during the second hour, any remaining melt is allowed to evaporate, reducing water retention and preventing refrosting before the next frosting cycle begins.

Optical Microscopy. A custom microscopy (Eclipse LV100, Nikon) setup was used to observe atmospheric water vapor condensation and frosting-defrosting behavior of samples. The setup consists of a cold stage (TP104SC-mk2000A, Instec) and a high-resolution camera (Nikon) connected to an optical microscope. 47,58 The cold stage cools the sample surface to 5 \pm 0.5 °C for condensation or $-15~\pm~0.5$ °C for frosting experiments. For defrosting, surfaces were heated to 20 \pm 0.5 °C at a heating rate of 5 °C/min. The phase change phenomenon was recorded at 4 fps using 20× and 50× objective lenses (TU Plan Fluor EPI, Nikon), and a LED light source (SOLA SM II Light Engine, Lumencor) was selected for illumination, which has high intensity but low power consumption (2.5 W), which minimizes heat generation on the surface due to light absorption. The amount of light energy was controlled by adjusting the condenser aperture diaphragm opening

UV Exposure Testing. The UV exposure tests were carried out by putting the samples in a UV cleaner (FB-UVXL-1000, Fisher Scientific). The samples were kept in a glass beaker and placed inside the UV cleaner. During the test, the UV energy level was kept constant at 9000 μ J/cm².

Outdoor Weathering Testing. To assess the robustness of the surfaces in outdoor conditions, samples were exposed to outdoor ambient conditions for 1 month in summer (July 2021, Urbana, IL) and 1 month in winter (February 2022, Urbana, IL). The samples were six SHPo CuO coupons (5 cm × 5 cm), attached at a 45° angle to a metal plate, facing south in an open field for exposure to sunlight, wind, rain, snow, and air-borne dust particles. In summer, the samples were removed after 5, 10, 15, 20, 25, and 30 days. In winter, five samples were used and removed after the same intervals, with the fifth sample removed after 8 days.

X-ray Photoelectron Spectroscopy (XPS). XPS was performed using a monochromatic Al Ka source (Kratos Axis Ultra, Kratos Analytical). The size of the source beam was 2 mm × 2 mm, and the size of the analyzed region was 0.3 mm \times 0.7 mm. The instrument was maintained at a pressure of 10^{-7} Pa during the experiments. The spectra were postprocessed with CasaXPS software to determine the change in the composition of sample surfaces.

Scanning Electron Microscopy (SEM). Low- and highresolution field-emission scanning electron microscopy (FESEM) images of each sample were obtained using an FEI Quanta 450 ESEM in high-vacuum operation mode. The accelerating voltage was set to 5 kV, and the emission current was approximately 30 pA with a spot size of 2 nm to prevent charging and sample damage by the electron beam.

Water Droplet Advancing and Receding Contact Angles. Contact angle measurements of ≈100 nL water droplets on all samples were performed using a microgoniometer (MCA-3, Kyowa Interface Science). The advancing and receding contact angles were measured at multiple spots on each sample. For each sample, five measurements were taken at distinct locations and the results were averaged. To grow droplets, the piezoelectric dispenser was placed above each surface with a spacing from 5 to 10 mm and turned on to dispense monodisperse microscale droplets. The surface-dispenser

spacing was chosen to have close control of the dispensed droplet trajectory, which is not possible at larger spacings due to the presence of random air currents that act to deflect microscale droplets. Droplets were injected at a rate of 60-80 droplets/s. Due to the relatively small size of departing droplets (\sim 5 μ m), the shape of droplets remained spherical during flight. This assumption is justified given that the Bond, Weber, and capillary numbers are all much less than one. As the microscale droplets landed on the surface, they began to accumulate and grew to form a single larger droplet. The camera focal plane was located at the growing droplet midplane for the desired optical zoom level. Simultaneously, while the droplet was growing, contact angle measurements on the surface were performed. All contact angle data were analyzed using image processing software (FAMAS, interFAce Measurement and Analysis System) by the circle fitting method.

ASSOCIATED CONTENT

Supporting Information

The Supporting Information is available free of charge at https://pubs.acs.org/doi/10.1021/acsami.2c21928.

Actuation unit for the cycling experimental setup (Section S1), condensation and frosting experiments (Section S2), UV radiation (Section S3), XPS analysis of different SHPo surfaces (Section S4), fabrication of alternate antifrosting surfaces (Section S5), robustness and surface chemistry of the superhydrophilic surface (Section S6), thermal cycling (Section S7), and optical profilometry (Section S8) (PDF)

AUTHOR INFORMATION

Corresponding Authors

Xiao Yan - Department of Mechanical Science and Engineering, University of Illinois, Urbana, Illinois 61801, United States; Present Address: Department of Mechanical and Aerospace Engineering, the Hong Kong University of Science and Technology, Hong Kong 999077, China; Email: yan-x13@tsinghua.org.cn

Nenad Miljkovic - Department of Mechanical Science and Engineering, University of Illinois, Urbana, Illinois 61801, United States; Materials Research Laboratory and Department of Electrical and Computer Engineering, University of Illinois, Urbana, Illinois 61801, United States; International Institute for Carbon Neutral Energy Research (WPI-I2CNER), Kyushu University, Fukuoka 819-0395, *Japan*; © orcid.org/0000-0002-0866-3680; Email: nmiljkov@illinois.edu

Authors

Muhammad Jahidul Hoque - Department of Mechanical Science and Engineering, University of Illinois, Urbana, Illinois 61801, United States; o orcid.org/0000-0002-8036-4511

Haoyun Qiu - Department of Mechanical Science and Engineering, University of Illinois, Urbana, Illinois 61801, United States

Yimeng Qin - Department of Mechanical Science and Engineering, University of Illinois, Urbana, Illinois 61801, United States

Xuzhi Du - Department of Mechanical Science and Engineering, University of Illinois, Urbana, Illinois 61801, United States

Jackson Stermer - Department of Mechanical Science and Engineering, University of Illinois, Urbana, Illinois 61801, United States

Complete contact information is available at: https://pubs.acs.org/10.1021/acsami.2c21928

Author Contributions

[#]M.J.H., X.Y., and H.Q. contributed equally to this paper. X.Y. and N.M. conceived the idea for the work and guided the work. M.J.H., X.Y., H.Q., and Y.Q. built the experimental setup. Sample fabrication was carried out by M.J.H., X.Y., and H.Q. Sample characterizations and experiments were carried out by M.J.H., X.Y., H.Q., and X.D. Data analysis was carried out by M.J.H., X.Y., H.Q., and J.S. with the help of N.M. M.J.H., X.Y., H.Q., and N.M. discussed the results and wrote the manuscript. All authors read and approved the submission of the manuscript.

Notes

The authors declare no competing financial interest.

ACKNOWLEDGMENTS

Scanning electron microscopy and X-ray photoelectron spectroscopy (XPS) were carried out in the Materials Research Laboratory Central Facilities, University of Illinois. The authors thank Dr. Richard T. Haasch at the Materials Research Laboratory at the University of Illinois for their assistance in material characterizations and insightful discussions. M.J.H., X.Y., and N.M. gratefully acknowledge funding support from the Office of Naval Research (ONR) under grant No. N00014-16-1-2625 and the Advanced Research Projects Agency-Energy (ARPA-E) under grant No. DOE DE-AR0001594. N.M. also gratefully acknowledges funding support from the International Institute for Carbon Neutral Energy Research (WPI-I2CNER), sponsored by the Japanese Ministry of Education, Culture, Sports, Science and Technology. This research was partially supported by the NSF through the University of Illinois at Urbana-Champaign Materials Research Science and Engineering Center (DMR-1720633).

REFERENCES

- (1) Chavan, S.; Boyina, K.; Li, L.; Miljkovic, N. Recent Advances in Frosting for Heat Transfer Applications. In Nanoscale Energy Transport: Emerging Phenomena, Methods and Applications; IOP Publishing Ltd., 2020; pp 15-11-15-30.
- (2) Zhang, S.; Huang, J.; Cheng, Y.; Yang, H.; Chen, Z.; Lai, Y. Bioinspired Surfaces with Superwettability for Anti-Icing and Ice-Phobic Application: Concept, Mechanism, and Design. Small 2017, 13, No. 1701867.
- (3) Huang, X.; Tepylo, N.; Pommier-Budinger, V.; Budinger, M.; Bonaccurso, E.; Villedieu, P.; Bennani, L. A Survey of Icephobic Coatings and Their Potential Use in a Hybrid Coating/Active Ice Protection System for Aerospace Applications. Prog. Aerosp. Sci. 2019, 105, 74-97.
- (4) Shen, Y. Z.; Wu, X. H.; Tao, J.; Zhu, C. L.; Lai, Y. K.; Chen, Z. Icephobic Materials: Fundamentals, Performance Evaluation, and Applications. Prog. Mater. Sci. 2019, 103, 509-557.
- (5) Wang, F.; Liang, C.; Zhang, X. Research of Anti-Frosting Technology in Refrigeration and Air Conditioning Fields: A Review. Renewable Sustainable Energy Rev. 2018, 81, 707-722.
- (6) Rafati Nasr, M.; Fauchoux, M.; Besant, R. W.; Simonson, C. J. A Review of Frosting in Air-to-Air Energy Exchangers. Renewable Sustainable Energy Rev. 2014, 30, 538-554.
- (7) Kim, K.; Kim, M.-H.; Kim, D. R.; Lee, K.-S. Thermal Performance of Microchannel Heat Exchangers According to the Design Parameters Under the Frosting Conditions. Int. J. Heat Mass Transfer 2014, 71, 626-632.

- (8) Frankenstein, S.; Tuthill, A. M. Ice Adhesion to Locks and Dams: Past Work; Future Directions. *J. Cold Reg. Eng.* **2002**, *16*, 83–96
- (9) Lv, J. Y.; Song, Y. L.; Jiang, L.; Wang, J. J. Bio-Inspired Strategies for Anti-Icing. ACS Nano 2014, 8, 3152–3169.
- (10) Guo, L.; Zhou, L.; Chen, M.; Huang, W. Online Catenary Antiicing Technique for Electric Railways Employing Direct Feeding Systems. *IET Gener., Transm., Distrib.* **2016**, *10*, 1969–1975.
- (11) Parent, O.; Ilinca, A. Anti-icing and De-icing Techniques for Wind Turbines: Critical Review. *Cold Reg. Sci. Technol.* **2011**, *65*, 88–96.
- (12) Chang, S. E.; McDaniels, T. L.; Mikawoz, J.; Peterson, K. Infrastructure Failure Interdependencies in Extreme Events: Power Outage Consequences in the 1998 Ice Storm. *Nat. Hazards* **2007**, *41*, 337–358.
- (13) Siegel, A. F. E. a. B. L. Experimental Measurements of the Effects of Frost Formation on Heat Exchanger Performance. *ASME Heat Transfer Div.* **1990**, *139*, 1–7.
- (14) Huang, L.; Liu, Z.; Liu, Y.; Gou, Y.; Wang, J. Experimental Study on Frost Release on Fin-and-Tube Heat Exchangers by Use of a Novel Anti-Frosting Paint. *Exp. Therm. Fluid Sci.* **2009**, *33*, 1049–1054.
- (15) Laforte, J. L.; Allaire, M. A.; Laflamme, J. State-of-the-Art on Power Line De-Icing. *Atmos. Res.* **1998**, *46*, 143–158.
- (16) Makkonen, L. Ice Adhesion —Theory, Measurements and Countermeasures. J. Adhes. Sci. Technol. 2012, 26, 413–445.
- (17) Zhang, H. Y.; Yang, Y. L.; Pan, J. F.; Long, H.; Huang, L. S.; Zhang, X. K. Compare Study between Icephobicity and Superhydrophobicity. *Phys. B* **2019**, *556*, 118–130.
- (18) Boinovich, L.; Emelyanenko, A. M.; Pashinin, A. S. Analysis of Long-Term Durability of Superhydrophobic Properties under Continuous Contact with Water. *ACS Appl. Mater. Interfaces* **2010**, *2*, 1754–1758.
- (19) Liu, Q.; Yang, Y.; Huang, M.; Zhou, Y.; Liu, Y.; Liang, X. Durability of a Lubricant-Infused Electrospray Silicon Rubber Surface as an Anti-Icing Coating. *Appl. Surf. Sci.* **2015**, 346, 68–76.
- (20) Varanasi, K. K.; Deng, T.; Smith, J. D.; Hsu, M.; Bhate, N. Frost Formation and Ice Adhesion on Superhydrophobic Surfaces. *Appl. Phys. Lett.* **2010**, *97*, No. 234102.
- (21) Na, B.; Webb, R. L. A Fundamental Understanding of Factors Affecting Frost Nucleation. *Int. J. Heat Mass Transfer* **2003**, *46*, 3797–3808.
- (22) Sun, X.; Rykaczewski, K. Suppression of Frost Nucleation Achieved Using the Nanoengineered Integral Humidity Sink Effect. *ACS Nano* **2017**, *11*, 906–917.
- (23) Kulinich, S. A.; Farzaneh, M. Ice Adhesion on Super-Hydrophobic Surfaces. *Appl. Surf. Sci.* **2009**, 255, 8153–8157.
- (24) Meuler, A. J.; Smith, J. D.; Varanasi, K. K.; Mabry, J. M.; McKinley, G. H.; Cohen, R. E. Relationships between Water Wettability and Ice Adhesion. *ACS Appl. Mater. Interfaces* **2010**, *2*, 3100–3110.
- (25) Farhadi, S.; Farzaneh, M.; Kulinich, S. A. Anti-Icing Performance of Superhydrophobic Surfaces. *Appl. Surf. Sci.* **2011**, 257, 6264–6269.
- (26) Boinovich, L. B.; Emelyanenko, A. M.; Emelyanenko, K. A.; Modin, E. B. Modus Operandi of Protective and Anti-icing Mechanisms Underlying the Design of Longstanding Outdoor Icephobic Coatings. *ACS Nano* **2019**, *13*, 4335–4346.
- (27) Lazauskas, A.; Guobienė, A.; Prosyčevas, I.; Baltrušaitis, V.; Grigaliūnas, V.; Narmontas, P.; Baltrušaitis, J. Water Droplet Behavior on Superhydrophobic Sio2 Nanocomposite Films During Icing/Deicing Cycles. *Mater. Charact.* **2013**, 82, 9–16.
- (28) Wang, F.; Li, C.; Lv, Y.; Lv, F.; Du, Y. Ice Accretion on Superhydrophobic Aluminum Surfaces Under Low-Temperature Conditions. *Cold Reg. Sci. Technol.* **2010**, *62*, 29–33.
- (29) Guo, P.; Zheng, Y.; Wen, M.; Song, C.; Lin, Y.; Jiang, L. Icephobic/Anti-Icing Properties of Micro/Nanostructured Surfaces. *Adv. Mater.* **2012**, 24, 2642–2648.

- (30) Ling, E. J. Y.; Uong, V.; Renault-Crispo, J. S.; Kietzig, A. M.; Servio, P. Reducing Ice Adhesion on Nonsmooth Metallic Surfaces: Wettability and Topography Effects. *ACS Appl. Mater. Interfaces* **2016**, *8*, 8789–8800.
- (31) Boreyko, J. B.; Collier, C. P. Delayed Frost Growth on Jumping-Drop Superhydrophobic Surfaces. *ACS Nano* **2013**, *7*, 1618–1627.
- (32) Antonini, C.; Innocenti, M.; Horn, T.; Marengo, M.; Amirfazli, A. Understanding the Effect of Superhydrophobic Coatings on Energy Reduction in Anti-Icing Systems. *Cold Reg. Sci. Technol.* **2011**, *67*, 58–67
- (33) Zhang, Y.; Yu, X.; Wu, H.; Wu, J. Facile Fabrication of Superhydrophobic Nanostructures on Aluminum Foils with Controlled-Condensation and Delayed-Icing Effects. *Appl. Surf. Sci.* **2012**, 258, 8253–8257.
- (34) Chaudhary, G.; Li, R. Freezing of Water Droplets on Solid Surfaces: An Experimental and Numerical Study. *Exp. Therm. Fluid Sci.* **2014**, *57*, 86–93.
- (35) Zhang, H.; Zhao, Y.; Lv, R.; Yang, C. Freezing of Sessile Water Droplet for Various Contact Angles. *Int. J. Therm. Sci.* **2016**, *101*, 59–67
- (36) Chavan, S.; Park, D.; Singla, N.; Sokalski, P.; Boyina, K.; Miljkovic, N. Effect of Latent Heat Released by Freezing Droplets during Frost Wave Propagation. *Langmuir* **2018**, *34*, 6636–6644.
- (37) Tourkine, P.; Le Merrer, M.; Quere, D. Delayed Freezing on Water Repellent Materials. *Langmuir* **2009**, 25, 7214–7216.
- (38) Chavan, S.; Carpenter, J.; Nallapaneni, M.; Chen, J. Y.; Miljkovic, N. Bulk Water Freezing Dynamics on Superhydrophobic Surfaces. *Appl. Phys. Lett.* **2017**, *110*, No. 041604.
- (39) Shen, Y.; Wang, G.; Tao, J.; Zhu, C.; Liu, S.; Jin, M.; Xie, Y.; Chen, Z. Anti-Icing Performance of Superhydrophobic Texture Surfaces Depending on Reference Environments. *Adv. Mater. Interfaces* **2017**, *4*, No. 1700836.
- (40) Bengaluru Subramanyam, S.; Kondrashov, V.; Ruhe, J.; Varanasi, K. K. Low Ice Adhesion on Nano-Textured Superhydrophobic Surfaces under Supersaturated Conditions. *ACS Appl. Mater. Interfaces* **2016**, *8*, 12583–12587.
- (41) Chen, J.; Liu, J.; He, M.; Li, K.; Cui, D.; Zhang, Q.; Zeng, X.; Zhang, Y.; Wang, J.; Song, Y. Superhydrophobic Surfaces Cannot Reduce Ice Adhesion. *Appl. Phys. Lett.* **2012**, *101*, No. 111603.
- (42) Rykaczewski, K.; Anand, S.; Subramanyam, S. B.; Varanasi, K. K. Mechanism of Frost Formation on Lubricant-Impregnated Surfaces. *Langmuir* **2013**, *29*, 5230–5238.
- (43) Kulinich, S. A.; Farzaneh, M. How Wetting Hysteresis Influences Ice Adhesion Strength on Superhydrophobic Surfaces. *Langmuir* **2009**, 25, 8854–8856.
- (44) Schutzius, T. M.; Jung, S.; Maitra, T.; Eberle, P.; Antonini, C.; Stamatopoulos, C.; Poulikakos, D. Physics of Icing and Rational Design of Surfaces with Extraordinary Icephobicity. *Langmuir* **2015**, *31*, 4807–4821.
- (45) Miljkovic, N.; Enright, R.; Nam, Y.; Lopez, K.; Dou, N.; Sack, J.; Wang, E. N. Jumping-droplet-enhanced condensation on scalable superhydrophobic nanostructured surfaces. *Nano Lett.* **2013**, *13*, 179–187.
- (46) Hoque, M. J.; Yan, X.; Keum, H.; Li, L.; Cha, H.; Park, J. K.; Kim, S.; Miljkovic, N. High-Throughput Stamping of Hybrid Functional Surfaces. *Langmuir* **2020**, *36*, 5730–5744.
- (47) Yan, X. H. Z.; Huang, Z.; Sett, S.; Sett, S.; Oh, J.; Oh, J.; Cha, H.; Cha, H.; Li, L.; Li, L.; Feng, L.; Feng, L.; Wu, Y.; Wu, Y.; Zhao, C.; Zhao, C.; Orejon, D.; Orejon, D.; Chen, F.; Chen, F.; Miljkovic, N. Atmosphere-Mediated Superhydrophobicity of Rationally Designed Micro/Nanostructured Surfaces. *ACS Nano* **2019**, *13*, 4160–4173.
- (48) Yang, Z.; Wu, Y. Z.; Ye, Y.-F.; Ye, Y. F.; Gong, M.-G.; Gong, M. G.; Xu, X.-L. A simple way to fabricate an aluminum sheet with superhydrophobic and self-cleaning properties. *Chin. Phys. B* **2012**, *21*, 126801–126806.
- (49) Wang, R.; Guo, J.; Muckleroy, E. A.; Antao, D. S. Robust Silane Self-Assembled Monolayer Coatings on Plasma-Engineered Copper

- Surfaces Promoting Dropwise Condensation. Int. J. Heat Mass Transfer 2022, 194, No. 123028.
- (50) Wang, R.; Jakhar, K.; Ahmed, S.; Antao, D. S. Elucidating the Mechanism of Condensation-Mediated Degradation of Organofunctional Silane Self-Assembled Monolayer Coatings. ACS Appl. Mater. Interfaces 2021, 13, 34923-34934.
- (51) Nath, S.; Ahmadi, S. F.; Boreyko, J. B. A Review of Condensation Frosting. Nanoscale Microscale Thermophys. Eng. **2017**, *21*, 81–101.
- (52) Dooley, J. B. Determination and Characterization of Ice Propagation Mechanisms on Surfaces Undergoing Dropwise Condensation. Ph.D. Thesis, Texas A & M, 2010.
- (53) Rahman, M. A.; Jacobi, A. M. Study of Frost Properties and Frost Melt Water Drainage on Microgrooved Brass Surfaces in Multiple Frost/Defrost/Refrost Cycles. Appl. Therm. Eng. 2014, 64, 453-461.
- (54) Xia, Y.; Zhong, Y.; Hrnjak, P. S.; Jacobi, A. M. Frost, Defrost, and Refrost and its Impact on the Air-Side Thermal-Hydraulic Performance of Louvered-Fin, Flat-Tube Heat Exchangers. Int. J. Refrig. 2006, 29, 1066-1079.
- (55) Tassou, S. A.; Datta, D.; Marriott, D. Frost formation and defrost control parameters for open multideck refrigerated food display cabinets. Proc. Inst. Mech. Eng., Part A 2001, 215, 213-222.
- (56) Adrian Bejan, J. V. C. V.; Jong, S. Lim. When to defrost a refrigerator, and when to rernove the scale from the heat exchanger of a power plant. Int. J. Heat Mass Transfer 1994, 37, 523-532.
- (57) Hoque, M. J.; Sett, S.; Yan, X.; Liu, D.; Rabbi, K. F.; Qiu, H.; Qureshi, M.; Barac, G.; Bolton, L.; Miljkovic, N. Life Span of Slippery Lubricant Infused Surfaces. ACS Appl. Mater. Interfaces 2022, 14,
- (58) Kim, M. K.; Cha, H.; Birbarah, P.; Chavan, S.; Zhong, C.; Xu, Y.; Miljkovic, N. Enhanced Jumping-Droplet Departure. Langmuir **2015**, *31*, 13452–13466.
- (59) Cha, H.; Wu, A.; Kim, M. K.; Saigusa, K.; Liu, A.; Miljkovic, N. Nanoscale-Agglomerate-Mediated Heterogeneous Nucleation. Nano Lett. 2017, 17, 7544-7551.
- (60) Boyina, K. S.; Mahvi, A. J.; Chavan, S.; Park, D.; Kumar, K.; Lira, M.; Yu, Y.; Gunay, A. A.; Wang, X.; Miljkovic, N. Condensation Frosting on Meter-Scale Superhydrophobic and Superhydrophilic Heat Exchangers. Int. J. Heat Mass Transfer 2019, 145, No. 118694.
- (61) Koszut, J.; Boyina, K.; Popovic, G.; Carpenter, J.; Wang, S.; Miljkovic, N. Superhydrophobic Heat Exchangers Delay Frost Formation and Reduce Defrost Energy Input of Aircraft Environmental Control Systems. Int. J. Heat Mass Transfer 2022, 189, No. 122669.
- (62) Mahvi, A. J.; Boyina, K.; Musser, A.; Elbel, S.; Miljkovic, N. Superhydrophobic Heat Exchangers Delay Frost Formation and Enhance Efficency of Electric Vehicle Heat Pumps. Int. J. Heat Mass Transfer 2021, 172, No. 121162.
- (63) Giese, A. C. Living with Our Sun's Ultraviolet Rays; Springer Science & Business Media, 2012.
- (64) Figgis, B.; Nouviaire, A.; Wubulikasimu, Y.; Javed, W.; Guo, B.; Ait-Mokhtar, A.; Belarbi, R.; Ahzi, S.; Rémond, Y.; Ennaoui, A. Investigation of Factors Affecting Condensation on Soiled Pv Modules. Sol. Energy 2018, 159, 488-500.
- (65) Weather, W. https://uv.willyweather.com/il/champaigncounty.html.
- (66) Deegan, R. D.; Bakajin, O.; Dupont, T. F.; Huber, G.; Nagel, S. R.; Witten, T. A. Capillary Flow as the Cause of Ring Stains from Dried Liquid Drops. Nature 1997, 389, 827-829.
- (67) Yunker, P. J.; Durian, D. J.; Yodh, A. G. Coffee Rings and Coffee Disks: Physics on the Edge. Phys. Today 2013, 66, 60-61.
- (68) Wong, T. S.; Kang, S. H.; Tang, S. K.; Smythe, E. J.; Hatton, B. D.; Grinthal, A.; Aizenberg, J. Bioinspired Self-Repairing Slippery Surfaces with Pressure-Stable Omniphobicity. Nature 2011, 477,
- (69) Yan, X. C. F.; Chen, F.; Zhang, X. Q.; Zhang, X.; Qin, Y. M.; Qin, Y.; Zhao, C. Y.; Zhao, C.; Sett, S.; Sett, S.; Cha, H.; Cha, H.; Hoque, M. J.; Hoque, M. J.; Zhao, F. L.; Zhao, F.; Huang, Z. Y.;

- Huang, Z.; Miljkovic, N. Atmosphere-Mediated Scalable and Durable Biphilicity on Rationally Designed Structured Surfaces. Adv. Mater. Interfaces 2020, 7, No. 2000475.
- (70) Sett, S.; Oh, J.; Cha, H.; Veriotti, T.; Bruno, A.; Yan, X.; Barac, G.; Bolton, L. W.; Miljkovic, N. Lubricant-Infused Surfaces for Low-Surface-Tension Fluids: The Extent of Lubricant Miscibility. ACS Appl. Mater. Interfaces 2021, 13, 23121-23133.
- (71) Lee, J.; Sett, S.; Miljkovic, N. In Situ Opto-Hydrodynamic Characterization of Lubricant-Infused Surface Degradation. Langmuir **2023**, *39*, *367*–*376*.
- (72) Ma, J.; Cha, H.; Kim, M. K.; Cahill, D. G.; Miljkovic, N. Condensation Induced Delamination of Nanoscale Hydrophobic Films. Adv. Funct. Mater. 2019, 29, No. 1905222.
- (73) Chavan, S.; Foulkes, T.; Gurumukhi, Y.; Boyina, K.; Rabbi, K. F.; Miljkovic, N. Pulse Interfacial Defrosting. Appl. Phys. Lett. 2019, 115, No. 071601.
- (74) Li, L.; Khodakarami, S.; Yan, X.; Fazle Rabbi, K.; Gunay, A. A.; Stillwell, A.; Miljkovic, N. Enabling Renewable Energy Technologies in Harsh Climates with Ultra-Efficient Electro-Thermal Desnowing, Defrosting, and Deicing. Adv. Funct. Mater. 2022, 32, No. 2201521.
- (75) Wang, Z.-J.; Kwon, D.-J.; Lawrence DeVries, K.; Park, J.-M. Frost Formation and Anti-Icing Performance of a Hydrophobic Coating on Aluminum. Exp. Therm. Fluid Sci. 2015, 60, 132-137.

□ Recommended by ACS

Temperature-Responsive, Femtosecond Laser-Ablated Ceramic Surfaces with Switchable Wettability for On-**Demand Droplet Transfer**

Jing Zheng, Zhongrong Zhou, et al. MARCH 01 2023 ACS APPLIED MATERIALS & INTERFACES

READ

Photothermal MOF-Based Multifunctional Coating with Passive and Active Protection Synergy

Cheng Ke, Weimin Liu, et al.

MARCH 15, 2023

ACS APPLIED ENGINEERING MATERIALS

READ 2

Photo-Thermal Superhydrophobic Sponge for Highly **Efficient Anti-Icing and De-Icing**

Bo Yu, Feng Zhou, et al.

JANUARY 15, 2023

LANGMUIR

READ 🗹

Multiple-Droplet Selective Manipulation Enabled by Laser-**Textured Hydrophobic Magnetism-Responsive Slanted** Micropillar Arrays with an Ultrafast Reconfiguration Rate

Sizhu Wu, Zhaoxin Lao, et al.

FERRUARY 12 2023

LANGMUIR

RFAD 1

Get More Suggestions >